Distinct Raindrop Size Distributions of Convective Inner- and Outer-Rainband Rain in Typhoon Maria (2018)

Xuwei Bao[1], Liguang Wu[2,*], Shuai Zhang[1], Qingqing Li[3], limin Lin[1], Binke Zhao[1], Dan Wu[1], Weizu Xia[4], Bin Xu[5]

1. Key Laboratory of Numerical Modeling for Tropical Cyclones, and Shanghai Typhoon Institute, China Meteorological Administration, Shanghai, China
2. Department of Atmospheric and Oceanic Sciences and Institute of Atmospheric Sciences, Fudan University, Shanghai, China
3. Nanjing University of Information Science and Technology, Nanjing, China
4. Shanghai Meteorological Bureau, China Meteorological Administration, Shanghai, China
5. National Meteorological Information Center, China Meteorological Administration, Beijing, China

May 18, 2020

Revised for *Journal of Geophysical Research: Atmospheres*

Corresponding author:
Dr. Liguang Wu
Department of Atmospheric and Oceanic Sciences & Institute of Atmospheric Sciences
Fudan University, Shanghai 200438, China
E-mail: liguangwu@fudan.edu.cn

This article has been accepted for publication and undergone full peer review but has not been through the copyediting, typesetting, pagination and proofreading process which may lead to differences between this version and the Version of Record. Please cite this article as doi: 10.1029/2020JD032482

Abstract

Unlike previous studies from a single disdrometer, this study investigates and compares the raindrop size distribution (RSD) characteristics of convective inner-rainband rain (CIR) and convective outer-ranband rain (COR) in Typhoon Maria (2018), simultaneously captured for the first time by a newly-established observational network including nine disdrometers in the northeastern Fujian Province of China. It is shown that the radar reflectivity for the CIR increases sharply with decreasing height below the melting layer, whereas it remains nearly unchanged for the COR. This suggests the dominance of collision–coalescence process in the CIR, i.e., the collection of small raindrops by larger ones as they fall. Thus, the surface-level CIR generally has far lower concentration of small raindrops and larger mean raindrop diameter than those previously found in the COR. Close to the tropical cyclone (TC) eyewall, it is found for the first time that although the raindrops are relatively large, the raindrop concentration is too low to yield a high rain rate. In contrast, high rain rates are concentrated at a distance of about 1.5–2.5 times the radius of maximum wind from the TC center, where there are appropriate normalized concentrations ($\log_{10}N_w$) and corresponding raindrop diameters. In addition, this study demonstrates differences between the CIR and COR in terms of the RSD evolution with increasing rain rate, and the radar reflectivity–rain rate (Z–R) and shape–slope (μ–Λ) relationships, and confirms the existence of different rain microphysics in various rain regions of a TC.

Keywords: Typhoon Maria, raindrop size distribution, rain microphysical characteristics, radial rain rate

1. Introduction

The spiral rainbands in tropical cyclones (TCs) can be generally categorized into inner and outer rainbands (Guinn and Schubert 1993; Wang 2009; Li and Wang 2012). The inner rainbands originate near the eyewall and are mainly within about 2–3 times the radius of maximum wind (2-3 RMW), where the TC inner-core dynamics dominate (Wang 2009; Houze 2010; Wang 2012; Moon and Nolan 2015). In contrast, outer (or distant) rainbands occur often outside the inner-core region, far from the intrinsic vortex dynamics of a TC (Houze 2010; Li and Wang 2012). Previous studies have indicated that inner and outer rainbands have different kinematic structures and features (Willoughby 1978; Montgomery and Kallenbach 1997; Black and Hallett 1999; Bogner et al. 2000; Hence and Houze 2008; Wang 2009; Li and Wang 2012; Wang 2012; Moon and Nolan 2015), leading to different cloud structures and rain microphysics (Houze 2010, 2014; Didlake and Kumjian 2017). As a fundamental property of rain microphysics, the raindrop size distribution (RSD) characteristics within the inner and outer rainbands have not yet been well investigated.

Previous studies focused on the climatic RSD features of TC rain in different oceanic basins, and identified that TC rain has a higher concentration of small raindrops than non-TC rain, probably to enhance evaporation near the ground (Jorgensen and Willis 1982; Tokay and Short 1996; Tokay et al. 2008; Bringi et al. 2003; Zhang et al. 2006; Chang et al. 2009; Kumari et al. 2014; Deo et al. 2016;

Janapati et al. 2017; Wen et al. 2018). However, the composite results of these studies may obscure different RSD characteristics in the various TC rainbands. In fact, several investigations have noticed different rain microphysics in different TC rainbands (Ulbrich and Lee 2002; Chen et al. 2012; Wang et al. 2016; Wu et al. 2018; Bao et al. 2019, hereafter Bao19). Unfortunately, these investigations were constrained by measurements from a single disdrometer, and could not simultaneously capture and compare the RSD characteristics of inner and outer TC rainbands. Thus, Bao19 suggested a dense disdrometer network to fully measure RSD characteristics in the various rainbands of a TC, to improve radar- and satellite-based quantitative precipitation estimation (QPE) algorithms for TC rain and microphysical parameterization schemes used in TC models (Marshall and Palmer 1948; Milbrandt and Yau, 2005; Thompson et al., 2015).

A new observational network including nine surface disdrometers was recently established by the China Meteorological Administration (CMA) in northeast Fujian Province in summer 2017 (Figure 1). Heavy TC rain was measured for the first time by the observational network when Typhoon Maria passed over the network on 11 July 2018, providing an opportunity to compare the RSD characteristics of its inner and outer rainbands. Different profiles of vertical velocity over inner- and outer-rainband regions, as found by Li and Wang (2012) and Wang (2012), may be responsible for different raindrop growth rates, size sorting, and ultimately surface-level RSD characteristics (Rosenfeld and Ulbrich 2003; Kumjian and Ryzhkov 2010). Thus, this study focuses on investigating whether there is also a high concentration of small raindrops in inner-rainband rain, as found by Wang et al. (2016). Note however that the disdrometer rain samples of Wang et al. (2016) were rather far from the TC center.

Section 2 introduces the data and methods adopted by this study. Convective structures are briefly discussed in section 3. Section 4 analyzes and discusses the RSD characteristics and evolution with increasing rain rate in the inner- and outer-rainband rain of Typhoon Maria, as well as the impact of raindrop concentration and diameter on the radial distribution of rain rate. The radar reflectivity–rain rate (Z–R) and shape–slope (μ–Λ) relationships of the inner- and outer-rainband rain are compared in section 5. Finally, conclusions are summarized in section 6.

2. Data and methods

2.1 Data

A new observational network including nine OTT second-generation Particle Size and Velocity (PARSIVEL; OTT Hydromet, Germany; Löffler-Mang and Joss 2000; Battaglia et al. 2010) disdrometers was established in summer 2017. Each disdrometer is collocated with a CMA automatic weather station (AWS) in northeast Fujian Province (listed in Table 1 and shown in Figure 2). Each disdrometer provides a two-dimensional matrix including 32 nonequidistant classes of particle diameter and 32 nonequidistant classes of fall speed at 1-minute sampling interval if rain occurs, with drop counts in the two smallest diameter classes set to zero because of the low signal-to-noise ratio (Löffler-Mang and Joss 2000; Yuter et al. 2006; Jaffrin and Berne 2011).

The heavy TC rain associated with Typhoon Maria was the first such event captured by the new observational network. Based on the CMA best track dataset, Typhoon Maria made landfall with a wind intensity of 42 m s^{-1} at Lianjiang in Fujian Province, China at around 0910 local standard time (LST) 11 July 2018, and finally dissipated (TC track no longer updated) at 2000 LST 11 July 2018 (Figure 1). Therefore, all disdrometers stopped sampling this event at 2000 LST 11 July 2018.

Other observational datasets used in this study include radar data collected by the China New Generation Doppler Weather Radar (CINRAD/SA) in Ningde, Fujian Province (blue triangle in Figure 2) and AWS data (e.g., surface rainfall). In general, accumulated rainfall >50 mm fell along the track of Typhoon Maria and over the southeastern coast of Zhejiang Province (Figure 1a).

2.2 Methods

As in Bao19, several quality control (QC) procedures suggested by previous studies (Atlas et al. 1973; Tokay and Bashor 2010; Jaffrain and Berne 2011; Friedrich et al. 2013) are applied to eliminate spurious raindrops before calculation of RSD parameters in this study. All RSD parameters and integrated rainfall variables (Appendix A) are calculated directly from the observed disdrometer data after QC, using the three-parameter gamma model introduced by Ulbrich (1983):

$$N(D) = N_0 D^{\mu} \exp(-\Lambda D), \quad (1)$$

where $N(D)$ is the number concentration of raindrop per unit volume and per unit size interval (mm^{-1} m^{-3}), and D is the equivalent raindrop diameter (mm); the intercept parameter N_0 (mm$^{-1-\mu}$ m^{-3}), shape parameter μ and slope parameter Λ (mm^{-1}) are the three parameters of the gamma model. As shown in Bao19, the rain rate derived from PARSIVEL disdrometer data is consistent with data from rain gauges (not shown).

The S-band radar deployed in Ningde, Fujian Province is situated at 138 m above sea level. The radar scans a three-dimensional volume within a radius of 230 km, with an approximately 1° beam width by 1-km range resolution, and 6-minute sampling frequency for a volume scan. Each volume scan consists of nine sweeps, with elevation angles ranging from 0.5° (base scan) to 19° (Kim et al. 2014). The radar reflectivity data used in this study was qualitatively controlled by a Severe Weather Now-casting System (Wu et al. 2013), and then the quality-controlled volume data is interpolated into Cartesian coordinates to obtain the constant altitude plan position indicator (CAPPI) data with horizontal (vertical) resolution of 1 km (500 m). The TC tracking radar echoes by correlation (T-TREC) technique developed by Wang et al. (2011) is applied to retrieve the wind field and calculate the RMW of Typhoon Maria (Figure 2). The outer-rainband region is defined as more than 3 RMW from the TC center and the inner-rainband region as within an annular region between the RMW and 3 RMW from the T-TREC wind field at an altitude of 2 km, as used by Li and Wang (2012).

The method for identifying the rain samples measured by each disdrometer as inner- or outer-rainband rain is introduced in Appendix B. Figure 3a highlights the convective rain region with radar reflectivity >32 dBZ in Figure 2c (Roger et al. 2013; Barnes and Barnes 2014). The inner rainbands are generally within 3 RMW, whereas the relatively narrow outer rainbands in which discrete convective cells embedded are located mainly outside 3 RMW. In addition, note that the convective elements with radar reflectivity > 32 dBZ isolated from the inner rainbands (excluding the linkage with inner rainbands) are herein categorized as outer-rainband convection (Figure 3a), despite being within 3 RMW. Based on the discrimination criteria in Appendix B, consequently, the rain duration for the resultant inner- or outer-rainband rain observed by each disdrometer is listed in Table 1. Based on disdrometer measurements, a modified classification method of convective and stratiform rain types is adopted in this study, which was examined more applicable in TC rain and whose detailed discussion can been found in Bao19.

3. Structure of radar reflectivity

Figure 3b displays the average radius–height cross section of radar reflectivity approximately transecting the inner and outer rainbands (IR and OR) as indicated by Figure 2a at 0400 LST 11 July 2018. Stratiform rain (characterized by the bright-band signature) dominates within the RMW as expected, whereas a strong convective rainband is located in the inner-rainband region, and the outer rainband is outside 3 RMW. The reflectivity of the inner rainband increases markedly as height decreases below 4 km (Figure 3b). Even when the inner rainbands approached the land at other times, the reflectivity still exhibits the increase with decreasing height (not shown). Thus this can be a reliable signal of the collision-coalescence process of raindrops as they fall in inner rainbands (Kumjian and Prat 2014; Seela et al. 2018).

To compare the structures of radar reflectivity for the convective inner-rainband rain (CIR) and convective outer-rainband rain (COR) captured by the new observational network, Figure 4 shows the contoured frequency by altitude diagrams (CFADs) of radar reflectivity for the CIR and COR. This is derived by compositing the CAPPI radar reflectivity over the disdrometers that measured rain samples of the CIR (or COR). For the CIR, the average radar reflectivity increases above an altitude of 9 km, as does its contoured frequency >20% (shading in Figure 4). This is not the case for the COR. This may partly result from slantwise convection that originates from the TC eyewall just above the inner rainbands, as indicated by Didlake and Houze (2013). Thus, Figure 4 does not reveal the real convection-top height of the inner rainbands in this study. As shown in Figure 3b, the average reflectivity of the CIR increases pronouncedly with decreasing height below the melting layer, whereas it remains nearly unchanged for the COR (Figure 4). This can be attributed to stronger area-averaged ascending motion associated with convergence at the middle and lower troposphere over the convective inner-rainband region, whereas area-averaged downward motion is found below 4-km height over the convective outer-rainband region, as found by Li and Wang (2012).

Figure 5 shows scatterplots of surface rain rate versus distance from the TC center for the CIR and COR as the inner and outer rainbands (Figure 2) passed over the observational network from 0330 LST to 0700 LST 11 July 2018. In general, the CIR has more samples with a high rain rate than the COR, corresponding to a larger low-level average reflectivity for the CIR (Figure 4). Therefore, this study examines whether the different convection structures of the CIR and COR result in different surface-level RSD characteristics. In addition, Figure 5 shows that the largest rain rate occurs at 90–120 km from the TC center, far from the eyewall (which is about 50 km from the TC center). This behavior is investigated in the following section.

4. RSD characteristics

4.1 Composite RSD

Using the modified rain-type classification method of Bao19, 593 (486) samples are classified as convective rain in the inner-rainband (outer-rainband) region of Typhoon Maria (Table 2). The mean integrated rainfall parameters show that the CIR has a larger rain rate, rain water content and mass-weighted mean raindrop diameter, but lower raindrop concentration, than the COR (Table 2). This is confirmed by the scatterplots of D_m versus $\log_{10}N_w$ overlaid with the contours of rain rate (Figure 6a). The CIR has more samples in the region with large D_m (smaller $\log_{10}N_w$) and high rain rate than the COR. In contrast, there are a fair number of samples in the COR with $\log_{10}N_w > 4.5$ mm^{-1} m^{-3}, but corresponding $D_m < 1.5$ mm (Figure 6a). As a result, the COR of Typhoon Maria has a similar mean value of D_m (1.51 mm) to those reported by Wang et al. (2016) and Bao19, but the CIR has a larger D_m (1.72 mm). This is consistent with the larger radar reflectivity for the CIR at low levels than for the COR in this study (Figure 4).

Figure 6b shows the composite raindrop spectra for the CIR and COR. Although the CIR and COR almost have the same spectral width, the CIR has far lower concentrations of small raindrops, but more midsize (especially 2–3 mm) raindrops than the COR (Figure 6b). Tokay et al. (2008) found that midsize raindrops make a significant contribution to the rain rate of heavy rain. Thus, the CIR has a larger mean rain rate than the COR (Table 2).

Previous studies have argued that the larger D_m of TC rainfall in Taiwan compared with that in mainland China is due to the lifting effect of the Central Mountain Range (Chang et al. 2009). Although it is still difficult to derive vertical velocity directly from the network (lack of relevant detection instruments or retrieval technology from single radar) in this study, previous high-resolution numerical simulations had found the stronger vertical updraft over the convective inner-rainband region than over the convective outer-rainband region (Li and Wang 2012; Wang 2012). This result may be used to account for the larger D_m for the CIR than for the COR in this study, because the ascending motion can lift small raindrops upward to grow into larger raindrops or hold them aloft to be collected by large raindrops via collision-coalescence process (Seela et al. 2018). This is reflected in the increasing radar reflectivity with decreasing height below the melting layer (Kumjian and Prat 2014), as shown in Figure 4. Warm-rain process dominates the inner-rainband rain, in agreement with Wang et al. (2016). In contrast, area-averaged downward vertical mass transport was found below 4-km height over the outer-rainband region by Li and Wang (2012). Thus, the small raindrops of the COR fall directly to the ground, leading to more small raindrops than in the CIR (Figure 6b).

In summary, the CIR has a larger average rain rate and raindrop diameter than the COR, likely because of collision-coalescence process associated with mid-to-low-level updraft over the inner-rainband region (Li and Wang 2012; Wang et al. 2016). Figure 6b shows that the COR has a higher concentration of small raindrops than the CIR at lower rain rates (<10 mm h^{-1}), similar to the findings of Bao19. Thus, the evolution of RSD with increasing rain rates will be discussed next.

4.2 RSD evolution with increasing rain rate

Figures 7a–b show the evolution of RSD in the CIR and COR as the rain rate increases for four rain-rate classes: 5–10 mm h^{-1} (moderate rain), 10–15 mm h^{-1} (moderate-to-heavy rain), 15–30 mm h^{-1} (heavy rain), and >30 mm h^{-1} (torrential rain). In general, the concentrations at all drop sizes increase monotonically with increasing rain rate in the CIR (Figure 7a). This is similar to the findings of several previous studies of weather systems other than TCs (Testud et al. 2001; Niu et al. 2010; PorCù et al. 2014; Bao19), which found that the increase of both raindrop size and concentration contribute to the increase of rain rate. A common feature of previous studies is that the initial concentration of small raindrops is not high, far less than that in the outer rainbands in either Bao19 or this study. In the COR, for rain rates <30 mm h^{-1}, the concentrations of raindrops <1 mm remain nearly unchanged with increasing rain rate, whereas the concentrations of other drop sizes increase. This suggests that the concentrations of small raindrops may saturate at the initial stage of convection. Once the rain rate exceeds 30 mm h^{-1}, the concentrations of tiny raindrops <0.7 mm suddenly increase and the raindrop spectrum (< 3 mm) takes the form of a double-peak model (Figure 7b), possibly due to the breakup process of large raindrops as discussed by previous studies (Zawadzki et al. 2001; Rosenfeld and Ulbrich 2003). Note that this double-peak model of raindrop spectrum (< 3 mm) does not occur in the CIR (Figure 7a). Previous studies have argued that raindrop concentration is not unlimited (Bringi et al. 2003; Wen et al. 2018). Thus, whether there is some threshold value of concentration of small raindrops at the initial stage of convection that can be used to determine the subsequent RSD evolution with increasing rain rate needs to be studied in the future.

Figures 7c–d show the ratios of deviation between RSD at the *j*th rain rate [$N(D_i)_j$] and the composite RSD [$N(D_i)_c$] with respect to the composite RSD [$N(D_i)_c$] at the *i*th drop size for the CIR and COR, as used in Bao19. The concentrations of almost all drop sizes in the CIR increase as the rain rate increases. However, the spectral lines of raindrops < 1 mm nearly overlap for the first three rain-rate classes in the COR, and even the concentrations of small raindrops at 10–15 mm h^{-1} are slightly higher than those at 15–30 mm h^{-1}. Once the rain rate exceeds 30 mm h^{-1}, the concentrations of tiny raindrops rise sharply, particularly for raindrops of diameter ~0.5 mm. The spectral lines for different rain-rate classes in both the CIR and COR are quite close near 4-mm drop diameters, because large (> 4 mm) raindrops are rarely measured in TC rain, as argued by previous studies (Tokay et al. 2008; Deo and Walsh 2016; Wen et al. 2018). In addition, this study confirms that the increasing rate of midsize raindrops is the greatest at high rain rates in both the CIR and COR, as first identified by Bao19.

The mean total concentrations and mean mass-weighted raindrop diameters for different rain-rate classes are shown in Figures 7e–f, along with the corresponding increase (percentage) between adjacent rain-rate classes. The COR generally has a higher mean total concentration and a smaller mean mass-weighted raindrop diameter than the CIR in each rain-rate class (Figures 7e–f). The COR has a smaller rate of increase of mean total concentration than the CIR in the first three rain-rate classes, but a higher rate of increase of mean raindrop diameter (Figures 7e–f). Once the rain rate exceeds 30 mm h^{-1}, the rate of increase of mean total concentration in the COR rises sharply (~53.1%), and starts to exceed that in the CIR. This is attributed to the rapid increase of tiny raindrops, possibly resulted from the breakup of large raindrops as discussed above. Therefore, this study confirms the argument of Bao19 that the increase of rain rate in COR is due to the growth of raindrop size rather than the increase of raindrop concentration at low rain-rate classes, possibly because the COR already has a very high concentration of raindrops at the initial stage of convection.

Area-averaged rain rate and raindrop diameter are larger in the CIR than in the COR, possibly due to the raindrop growth via collision–coalescence processes as the drops fall, as discussed above. Whether the rain rate and the raindrop diameter increase radially toward the TC center as the updraft increases, and whether the largest values occur close to the TC eyewall where the strongest updraft is located remain to be investigated as follows.

4.3 Radial characteristics of rain rate

Figure 8 shows the time-averaged $\log_{10}N_w$ (red), D_m (blue), and rain rate (purple) for the CIR and COR at each disdrometer site. The CIR usually has larger D_m (smaller $\log_{10}N_w$) than the COR, even when measured at the same disdrometer site. However, four disdrometer sites observed lower rain rates for the CIR than for the COR: Zhouning (2), Fuan (3), Fuding (5) and Pingnan (9) stations (Table 1; Figure 8). This means that although there is larger D_m for the CIR than for the COR, as measured at any one of these four sites, this does not necessarily result in larger rain rate. Figure 9 shows scatterplots and box plots of the radial distribution of D_m, $\log_{10}N_w$, and rain rate from all samples of the CIR and COR, with respect to the distance normalized by the RMW (r/RMW) from the TC center. Note that the rain produced by the single convective elements (with radar reflectivity >32 dBZ) isolated from the inner rainbands is categorized as COR, so the innermost location of COR samples is near 2.5 RMW (Figure 9). This implies the discrimination criteria for inner- or outer-rainband rain applied to this study should be appropriate. In general, the CIR has more samples with larger D_m and smaller $\log_{10}N_w$ than the COR, as shown in Figure 6a. Moreover, the closer to the TC center, the larger the mean D_m (Figure 9d), but the lower the mean $\log_{10}N_w$ (Figure 9e). The sample with largest D_m appears near 1–1.5 RMW from the TC center as expected, whereas the sample with highest $\log_{10}N_w$ is located 2.5–3.0 RMW from the TC center. In contrast, high rain rates exceeding 30 mm h^{-1} are concentrated near 1.5–2.5 RMW from the TC center (approximately upwind of inner rainbands). The rain near this area has a wide spread of D_m and $\log_{10}N_w$ (Figures 9d–f), which may be associated with more convective features in the upwind (outer) portion of inner rainbands, as argued by Didlake and Houze (2013). The reason why high rain rates occur mainly in this area and not close to the eyewall is discussed next.

Figure 10 shows scatterplots of rain rate versus $\log_{10}N_w$ from all samples (black points) after QC and those (red points) measured near 1.5–2.5 RMW from the TC center. The profile of maximum rain rate with respect to $\log_{10}N_w$ follows a normal distribution with mean 4.0 mm^{-1} m^{-3}. Rain rates >30 mm h^{-1} often require $\log_{10}N_w$ between 3.8 and 4.2 mm^{-1} m^{-3}, and most of these are located near 1.5–2.5 RMW from the TC center. From equation A5 in appendix A, the calculation of rain rate is associated with both the concentration and diameter of raindrops. Although most samples of CIR near 1–1.5 RMW from the TC center (close to the eyewall) have D_m > 1.5 mm (approximately the mean value for the COR; Table 2), the corresponding $\log_{10}N_w$ rarely exceeds 3.8 mm^{-1} m^{-3}. As a result, the rain rate close to the eyewall barely exceeds 30 mm h^{-1} (Figure 9). In contrast, in the area near 1.5–2.5 RMW from the TC center, the number of samples with $\log_{10}N_w$ > 3.8 mm^{-1} m^{-3} significantly increases (Figure 9), as do those with rain rates > 30 mm h^{-1} (Figure 10). These samples tend to have values of D_m and $\log_{10}N_w$ in the top right of the distribution as shown in Figure 6a.

The radial distributions of $\log_{10}N_w$, D_m and rain rate may be associated with the difference in dynamics with increasing radial distance from the TC center. As indicated by previous studies (Houze 2010; Li and Wang 2012; Wang 2012), there is a stronger mean updraft over the inner-rainband region than over the outer-rainband region, particularly close to the eyewall, leading to larger D_m and smaller $\log_{10}N_w$ in the CIR than in the COR (Table 2 and Figure 6a). There is mid-to-low-level rising motion over the inner-rainband region, as indicated by previous studies (Li and Wang 2012; Wang 2012), which may prevent small raindrops in the CIR from falling directly to the ground, particularly close to the TC eyewall (Narayana Rao et al. 2008;

Seela et al. 2018). This is why there is no double-peak structure in the raindrop spectra of the CIR, even for larger rain rates (Figure 7). This is also why most samples with D_m > 1.5 mm are found close to the eyewall (near 1–1.5 RMW from the TC center) in this study, even though the rain rate barely exceeds 30 mm h^{-1} because the raindrop concentration is too low (Figure 9). This may explain why extreme convection does not necessarily produce extreme rain rate, as argued by Hamada et al. (2015).

The COR has far fewer samples with D_m > 1.5 mm than the CIR, and thus the COR has fewer samples with rain rates > 30 mm h^{-1} than the CIR (Figure 9c). Although these COR samples have rather high raindrop concentrations, the absence of mid-to-low-level updraft over this area is not conducive to raindrop growth, consistent with the nearly unchanged radar reflectivity below the melting layer (Figure 4). Consequently, high rain rates often occur in the area near 1.5–2.5 RMW from the TC center, where the appropriate combination of raindrop concentration and raindrop size exist (Figs 9c and 10).

5. *Z*–*R* and *μ*–*Λ* relationships

The different RSD characteristics and evolution of the CIR and COR discussed in section 3 are bound to result in different *Z*–*R* relationships. Figure 11 shows scatterplots of *Z* versus *R* for the CIR and COR from this study, and the corresponding best-fit lines using the least square method, along with the composite results of seven typhoons reported by Wen et al. (2018) and the outer-rainband convective rain of Typhoon Fitow reported by Bao19. The larger D_m gives the CIR a larger coefficient (*A*

= 425.99) in this study. Although also classified as convective outer-rainband rain, the COR in this study has a larger coefficient (*A* = 237.58) than that of Typhoon Fitow, as reported by Bao19. This is possibly due to the longer distance between the disdrometer station and the TC center in Bao19, leading to more samples with small D_m in the convective outer-rainband rain of Typhoon Fitow. There is a similar discrepancy in the CIR between Wang et al. (2016) and this study, because the disdrometer is farther from the TC center in Wang et al. (2016). Note that although the composite relation reported by Wen et al. (2018) may represent the climatic characteristics of TCs making landfall in eastern China, it may smooth the variable characteristics in different rain regions of a single TC. Therefore, a variable *Z–R* relationship is suggested for radar and satellite QPE in different rain regions away from the TC center, based on the dense detecting network of disdrometers in eastern China used in this study.

The μ–Λ relationship has been widely used in the retrieval of RSDs derived from polarimetric radar data (Ulbrich 1983; Haddad et al. 1997; Zhang et al. 2001; Brandes et al. 2004; Cao et al. 2008). Figure 12 shows the scatterplots of μ versus Λ and corresponding best-fit lines for the CIR and COR with rain rates > 5 mm h^{-1} and the total concentration above 1000 m^{-3}, along with the results reported by Chang et al. (2009), Wen et al. (2018) and Bao19. In general, the fitting lines derived from data of this study are located between those reported by previous studies, and the CIR has a different μ–Λ relationship than the COR. For a given Λ, the CIR has a larger μ than the COR. The μ–Λ relationships in CIR and COR derived from this study are different from the composite results of previous studies, which hints the need to use a variable μ–Λ relationship to retrieve RSDs from polarimetric radar data in different rain regions of a TC.

6. Summary

To extend previous studies using a single disdrometer, this study investigated the RSD characteristics and evolution in convective inner-rainband rain (CIR) and convective outer-rainband rain (COR) of Typhoon Maria (2018), measured simultaneously for the first time by a newly established observational network including nine surface disdrometers in the northeastern Fujian Province of China. The focus was on investigating whether there is also high concentration of small raindrops in the CIR as found in previous studies of the COR, and the impact of raindrop concentration and diameter on the radial distribution of rain rate from the TC center.

It was demonstrated that the radar reflectivity for the CIR sharply increases as the altitude decreases below the melting layer, whereas it remains nearly unchanged for the COR. This result suggests raindrop growth via a collision–coalescence (warm-rain) process (the collection of small raindrops by larger ones as they fall) dominates in the CIR, as argued by previous studies.

Consequently, the CIR has more samples with large surface rain rates than the COR. Moreover, unlike previous findings, this study found that the CIR does not have a high concentration of small (<1 mm) raindrops, as does the COR, even though they have almost the same spectral width. In contrast, the CIR generally has more midsize (especially 2–3 mm) raindrops, accounting for larger integrated rain rate and mass-weighted mean raindrop diameter compared with the COR.

The radial distributions of rain rate, D_m and normalized intercept parameter $\log_{10}N_w$ from all samples after QC show for the first time that the closer to the TC center, the larger (smaller) the D_m ($\log_{10}N_w$). Despite the large D_m close to the TC eyewall, the rain rate barely exceeds 30 mm h^{-1} due to the low raindrop concentration ($\log_{10}N_w$ barely exceeds 3.8 mm^{-1} m^{-3}) in this area. In contrast, rain rates >30 mm h^{-1} occur mainly in the area near 1.5–2.5 RMW from the TC center (approximately upwind of inner rainbands), where appropriate values of $\log_{10}N_w$ (3.8–4.2 mm^{-1} m^{-3} in this study) and corresponding D_m exist. This may also explain why extreme convection does not necessarily produce extreme rain rates as argued by Hamada et al. (2015).

Different radar reflectivity–rain rate (Z–R) and shape–slope (μ–Λ) relationships are found in the CIR and COR, as well as different RSD evolution with increasing rain. The RSD evolution with increasing rain rate in the COR is in agreement with Bao19 in the outer rainbands, whereas in the CIR the raindrop concentrations at all drop sizes increase almost monotonically with increasing rain rate. Note that the double-peak distribution of the raindrop spectrum in the COR and Bao19 does not occur in the CIR, even when the rain rate has exceeded some threshold value.

Based on the measurement of TC rain derived from a newly established observational network, this study further demonstrates different rain microphysical characteristics in various rain regions away from the TC center, in agreement with previous studies. However, all the disdrometers were located on the right side of the track of Typhoon Maria, and did not collected all rainfall samples over the land. Thus, whether RSDs on the left side of the track also have the characteristics found in this study (whether the RSDs have azimuthal dependence) needs to be justified by further analysis of more TC cases in the future. In addition, the impact of vertical velocity on the radial RSD of TC rain needs to be investigated further through upgrading the network (e.g., implementing vertical-pointing radar), as well as the ability of high-resolution TC simulations in representing the impact of raindrop concentration and diameter on the rain rate with decreasing radius from a TC center in future work.

Acknowledgements

This study was supported jointly by the National Key R&D Program of China 2017YFE0107700 and 2018YFC1506400, the National Natural Science Foundation of China (41675051, 41705036, 41775064 and 41975069). General data used in this study can be found at open access http://data.cma.cn/en/?r=data/index, and public user can freely apply for an online account in accordance with the data policy of the China Meteorological Administration. The radar CAPPI and disdrometer data is available on http://pan.sti.org.cn/f/cf5496478f/. We thank the Editor and anonymous reviewers for their valuable comments that greatly improved the manuscript.

APPENDIX A

Calculation of rain parameters

Based on the three-parameter gamma model (Ulbrich 1983), the number concentration $N(D_i)$ of the ith size class (D_i) can be represented as follows:

$$N(D_i) = \sum_{j=1}^{32} \frac{n_{ij}}{A_{eff}(D_i) \cdot \Delta t \cdot V_j \cdot \Delta D_i}, \tag{A1}$$

where n_{ij} is the raindrop count at the ith size class and the jth velocity class recorded by the disdrometer; Δt is the sampling time (60 s); V_j (m s^{-1}) is the measured fall velocity at the jth velocity class; ΔD_i is the diameter interval at the ith size class; and $A_{eff}(D_i)$ (mm^2) is the effective sampling area at the ith size class (Battaglia et al. 2010; Jaffrain and Berne, 2011), which can be calculated as follows:

$$A_{eff}(D_i) = 180 \times (30 - \frac{D_i}{2}). \tag{A2}$$

Thus, several integrated rainfall parameters can be derived from $N(D_i)$ as follows:

$$N_t = \sum_{i=1}^{32} N(D_i) \Delta D_i, \tag{A3}$$

$$Z = \sum_{i=1}^{32} N(D_i) D_i^6 \Delta D_i, \tag{A4}$$

$$R = 6\pi \times 10^{-4} \sum_{i=1}^{32} \sum_{j=1}^{32} V_j N(D_i) D_i^3 \Delta D_i \text{, and} \tag{A5}$$

$$W = \frac{\pi \rho_w}{6} \sum_{i=1}^{32} N(D_i) D_i^3 \Delta D_i, \tag{A6}$$

where N_t is the total concentration of raindrops (m^{-3}); Z is the radar reflectivity factor (mm^6 m^{-3}), R is the rain rate (mm h^{-1}); W is the rain water content (g m^{-3}); $N(D_i)$ is the number concentration for the raindrop at the ith size class (D_i) as presented in Bao19; ρ_w is the density of water (1000 kg m^{-3}); V_j (m s^{-1}) is the measured fall velocity at the jth velocity class and ΔD_i is the diameter interval at the ith size class.

In addition, the nth-order moment, the mass-weighted mean diameter D_m (mm) and normalized intercept parameter N_w (mm^6 m^{-3}) (Ulbrich and Atlas 1998; Zhang et al. 2003) are defined as follows:

$$M_n = \int_0^{D_{\max}} D^n N(D)dD = \sum_{i=1}^{32} N(D_i)D_i^{\,n}\Delta D_i, \tag{A7}$$

$$D_m = \frac{M_4}{M_3}, \text{ and} \tag{A8}$$

$$N_w = \frac{256}{\pi\rho_w}\left(\frac{10^3 W}{D_m^4}\right), \tag{A9}$$

and N_0, μ, Λ of the gamma model are solved using the second, fourth, and sixth moments as suggested by Vievekanandan et al. (2004).

APPENDIX B

Discrimination between inner- and outer-rainband rain

The criteria used to discriminate whether the rain sample measured by any disdrometer is inner- or outer-rainband rain are as follows.

1) If the disdrometer site lies beneath the inner rainbands within ~3 RMW (outer rainbands outside ~3 RMW) both at the *i*th (T_i) and *i*+*6min*th (T_{i+6}) time, all seven samples measured by this disdrometer from T_i to T_{i+6} are categorized as inner-rainband (outer-rainband) rain.
2) If the disdrometer site lies beneath the inner rainbands at the *i*th (T_i) time, but beneath the outer rainbands at the *i*+*6min*th (T_{i+6}) time, the first four rain samples measured by this disdrometer from T_i to T_{i+3} are categorized as inner-rainband rain, and the last three from T_{i+4} to T_{i+6} are categorized as outer-rainband rain.
3) In contrast, if the disdrometer site is initially beneath the outer rainbands at the *i*th (T_i), but are beneath the inner rainbands at *i*+*6min*th (T_{i+6}), the first four (last three)

rain samples measured by this disdrometer from T_i to T_{i+3} (from T_{i+4} to T_{i+6}) are categorized as outer-rainband (inner-rainband) rain.

4) Outer rainbands are generally characterized by discrete convective elements with various organizational freedoms embedded within widespread stratiform precipitation region. Thus, if the disdrometer site is beneath a convective element with radar reflectivity > 32 dBZ (distinguishing the convective region suggested by Roger et al. 2013) isolated from the inner rainbands (excluding the linkage with inner rainbands), despite being within the inner edge of 3 RMW, all rain samples measured by this disdrometer from T_i to T_{i+6} are categorized as outer-rainband rain.

References

Atlas, D., R. C. Srivastava, and R. S. Sekhon, 1973: Doppler radar characteristics of precipitation at vertical incidence. *Rev. Geophys*., **11**, 1–35.

Bao, X., L. Wu, B. Tang, L. Ma, D. Wu, J. Tang, H. Chen and L. Wu, 2019: Variable Raindrop Size Distributions in Different Rainbands Associated with Typhoon Fitow (2013). *J. Geophys. Res. Atmos*., **124**. https://doi.org/10.1029/2019JD030268

Barnes, R. C., and G. M. Barnes, 2014: Eye and eyewall traits as determined with the NOAA WP-3D lower-fuselage radar. *Mon. Wea. Rev.*, **142**, 3393–3417.

Battaglia, A., E. Rustemeier, A. Tokay, U. Blahak, and C. Simmer, 2010: PARSIVEL snow observations: A critical assessment. *J. Atmos. Oceanic Technol.*, **27**, 333–344.

Black, R. A., and J. Hallett, 1999: Electrification of the hurricane. *J. Atmos. Sci.*, **56**, 2004–2028.

Bogner, P. B., G. M. Barnes, and J. L. Franklin, 2000: Conditional instability and shear for six hurricanes over the Atlantic Ocean. *Wea. Forecasting*, **15**, 192–207.

Brandes, E. A., G. Zhang, and J. Vivekanandan, 2004: Comparison of polarimetric radar drop size distribution retrieval algorithms. *J. Atmos. Oceanic Technol.*, **21**, 584–598.

Bringi, V. N., V. Chandrasekar, J. Hubbert, E. Gorgucci, W. L. Randeu, and M. Schoenhuber, 2003: Raindrop size distribution in different climatic regimes from disdrometer and dual-polarized radar analysis, *J. Atmos. Sci.*, **60**, 354–365.

Cao, Q., G. Zhang, E. Brandes, T. Schuur, A. Ryzhkov, and K. Ikeda 2008: Analysis of video disdrometer and polarimetric radar data to characterize rain microphysics in Oklahoma. *J. Appl. Meteorol. Climatol.*, **47**, 2238–2255.

Chang, W. -Y., T. -C. C. Wang, and P. -L. Lin, 2009: Characteristics of the raindrop size distribution and drop shape relation in typhoon systems in the Western Pacific from the 2D video disdrometer and NCU C-band polarimetric radar, *J. Atmos. Oceanic Technol.*, **26**, 1973–1993.

Chen, B., Y. Wang, and J. Ming, 2012: Microphysical characteristics of the raindrop size distribution in Typhoon Morakot (2009), *J. Trop. Meteorol.*, **18**, 162–171.

Chen, B., J. Yang, and J. Pu, 2013: Statistical characteristics of raindrop size distribution in the Meiyu season observed in eastern China, *J. Meteorol. Soc. Jpn.*, **91**, 215–227.

Didlake, A. C., Jr., and R. A. **Houze**, Jr., 2013: Convective-scale variations in the inner-core rainbands of a tropical cyclone. *J. Atmos. Sci.*, **70**, 504-523.

Didlake, A. C., Jr., G. M. Heymsfield, P. D. Reasor, and S. R. Guimond, 2017: Concentric eyewall asymmetries in Hurricane Gonzalo (2014) observed by airborne radar. *Mon. Wea. Rev.*, **145**, 729–749.

Friedrich, K., S. A. Higgins, F. J. Masters, and C. R. Lopez, 2013: Articulating and stationary PARSIVEL disdrometer measurements in conditions with strong winds and heavy rainfall. *J. Atmos. Oceanic Technol.*, **30**, 2063–2080.

Fovell, R. G., K. L. Corbosiero, and H. -C. Kuo, 2009: Cloud microphysics impact on hurricane track revealed in idealized experiments. *J. Atmos. Sci.*, **66**, 1764–1778.

Guinn, T. A., and W. H. Schubert, 1993: Hurricane spiral bands. *J. Atmos. Sci.*, **50**, 3380–3403.

Haddad, Z. S., D. A. Short, S. L. Durden, E. Im, S. Hensley, M. B. Grable, and R. A.Black, 1997a: A new parametrization of the raindrop size distribution. *IEEE* Trans. Geosci. Remote Sens., 35, 532–539.

Hamada, A., Y. N. Takayabu, C. Liu, and E. J. Zipser, 2015: Weak linkage between the heaviest rainfall and tallest storms. *Nat. Commun.*, **6**, 6213, doi:https://doi.org/10.1038/ncomms7213.

Hence, D. A., and R. A. Houze, 2008: Kinematic structure of convective-scale elements in the rainbands of Hurricanes Katrina and Rita (2005). *J. Geophys. Res.*, **113**, D15108, doi:10.1029/2007JD009429.

Houze, R. A., 2010: Clouds in tropical cyclones. *Mon. Wea. Rev.*, **138**, 293–344.

Houze, R. A., 2014: *Cloud Dynamics*, 2nd Ed., Elsevier/Academic Press, Oxford, 432 pp.

Jaffrain, J., and A. Berne, 2011: Experimental quantification of the sampling uncertainty associated with measurements from PARSIVEL disdrometers. *Journal of Hydrometeorology*, **12**, 352–370.

Janapati, J., B. K. Seela, M. V. Reddy, K. K. Reddy, P. -L. Lin, T. N. Rao, and C. -Y. Liu, 2017: A study on raindrop size distribution variability in before and after landfall precipitations of tropical cyclones observed over southern India. *J. Atmospheric Sol.-Terr. Phys.*, **159,** 23-40.

Jorgensen, D. P., and P. T. Willis, 1982: A Z-R relationship for hurricanes. *J. Appl. Meteor.*, **21**, 356–366.

Löffler-Mang, M., and J. Joss, 2000: An optical disdrometer for measuring size and velocity of hydrometeors. *J. Atmos. Oceanic Technol.*, **17**, 130–139.

Kim J. -H., M. -L. Ou, J. -D. Park, K. R. Morris, M. R. Schwaller, and D. B. Wolff, 2014: Global Precipitation Measurement (GPM) ground validation (GV) prototype in the Korean Peninsula.J. *Atmos. Oceanic Technol.*, **31**, 1902–1921.

Kumjian, M. R., and A. V. Ryzhkov, 2012: The impact of size sorting on the polarimetric radar variables. *J. Atmos. Sci.*, **69,** 2042-2060.

Kumari, N., S. B. Kumar, J. Jayalakshmi, and K. K. Reddy, 2014: Raindrop size distribution variations in JAL and NILAM cyclones induced precipitation 2 observed over Kadapa (14.47 o N, 78.82 o E), a tropical semi-arid region of India. *Indian J. Radio Space Phys.*, **43**, 57-66.

Kumjian, M. R., and O. P. Prat, 2014: The impact of raindrop collisional processes on the polarimetric radar variables. *J. Atmos. Sci.*, 71, 3052–3067.

Li, Q., and Y. Wang, 2012: A comparison of inner and outer spiral rainbands in a numerically simulated tropical cyclone. *Mon. Wea. Rev.*, **140**, 2782–2805.

Marshall, J. S., and W. M. Palmer, 1948: The distribution of raindrops with size. *Journal of Meteorology*, **5**, 165-166.

May, P. T., 1996: The organization of convection in the rainbands of Tropical Cyclone Laurence. *Mon. Wea. Rev.*, **124**, 807–815.

McFarquhar, G. M., H. Zhang, G. Heymsfield, J. B. Halverson, R. Hood, J. Dudhia, and F. Marks Jr., 2006: Factors affecting the evolution of Hurricane Erin (2001) and the distributions of hydrometeors: Role of microphysical processes. *J. Atmos. Sci.*, **63**, 127–150.

Milbrandt, J., and M. Yau, 2005: A multimoment bulk microphysics parameterization. Part II: A proposed three-moment closure and scheme description, *J. Atmos. Sci.*, **62**, 3065–3081.

Montgomery, M. T., and R. J. Kallenbach, 1997: A theory for vortex Rossby-waves and its application to spiral bands and intensity changes in hurricanes. *Quart. J. Roy. Meteor. Soc.*, **123**, 435–465.

Moon, Y., and D. S. Nolan, 2010: The dynamic response of the hurricane wind field to spiral rainband heating. *J. Atmos. Sci.*, **67**, 1779–1805.

Narayana Rao, T., Radhakrishna, B., Srivastava, R., Mohan Satyanarayana, T., Narayana Rao, D., Ramesh, R., 2008. Inferring microphysical processes occurring in mesoscale convective systems from radar measurements and isotopic analysis. *Geophys. Res. Lett.* **35**, L09813, doi:10.1029/2008GL033495.

Niu, S., X. Jia, J. Sang, X. Liu, C. Lu, and Y. Liu, 2010: Distributions of raindrop sizes and fall velocities in a semiarid plateau climate: Convective versus stratiform rains. *J. Appl. Meteor. Climatol.*, **49**, 632–645.

Porcù, F., L. P. D'Adderio, F. Prodi, and C. Caracciolo, 2014: Rain drop size distribution over the Tibetan Plateau, *Atmos. Res.*, **150**, 21-30.

Rogers, R., P. Reasor, and S. Lorsolo, 2013: Airborne Doppler observations of the inner-core differences between intensifying and steady-state tropical cyclones. *Mon. Wea. Rev.*, **141**, 2970–2991.

Rosenfeld, D., and C. W. Ulbrich, 2003: Cloud microphysical properties, processes, and rainfall estimation opportunities, *Meteorol. Monogr.*, **30**, 237–258.

Seela B. K., J. Janapati, P. -L. Lin, P. K. Wang, and M. -T. Lee, 2018: Raindrop size distribution characteristics of summer and winter season rainfall over north Taiwan, *J. Geophys. Res. Atmos.*, **123**, 11,602–11,624.

Sharma, S., M. Konwar, D. K. Sarma, M. C. R. Kalapureddy, A. R. Jain, 2009: Characteristics of rain integral parameters during tropical convective, transition, and stratiform rain at Gadanki and its application in rain retrieval. *J. Appl. Meteorol. Climatol.* 48, 1245–1266.

Testud, J., S. Oury, R. A. Black, P. Amayenc, and X. Dou, 2001: The concept of "normalized" distribution to describe raindrop spectra: A tool for cloud physics and cloud remote sensing, *J. Appl. Meteorol.*, **40**, 1118–1140.

Thompson, E. J., S. A. Rutledge, B. Dolan, and M. Thurai, 2015: Drop size distributions and radar observations of convective and stratiform rain over the equatorial Indian and west Pacific Oceans. *J. Atmos. Sci.*, **72**, 4091–4125.

Tokay, A., and D. A. Short, 1996: Evidence from tropical raindrop spectra of the origin of rain from stratiform versus convective clouds, *J. Appl. Meteorol.*, **35**, 355–371.

Tokay, A., P. G. Bashor, E. Habib, and T. Kasparis, 2008: Raindrop size distribution measurements in tropical cyclones. *Mon. Wea. Rev.*, **136**, 1669–1685.

Tokay, A., and P. G. Bashor, 2010: An experimental study of small-scale variability of raindrop size distribution. *J. Appl. Meteor. Climatol.*, **49**, 2348–2365.

Ulbrich, C. W., 1983: Natural variations in the analytical form of the raindrop size distribution. *J. Climate Appl. Meteor.*, **22**, 1764–1775.

Ulbrich, C. W., and D. Atlas, 1998: Rainfall microphysics and radar properties: analysis methods for drop size spectra. *J. Appl. Meteor.*, **37**, 912–923.

Ulbrich, C. W., and L. G. Lee, 2002: Rainfall Characteristics Associated with the Remnants of Tropical Storm Helene in Upstate South Carolina. *Wea.*

Forecasting, **17**, 1257-1267.

Vivekanandan, J., G. Zhang, and E. Brandes, 2004: Polarimetric radar estimators based on a constrained gamma drop size distribution model, *J. Appl. Meteorol.*, **43**, 217–230.

Wang, M., K. Zhao, and D. Wu, 2011: The T-TREC technique for retrieving the winds of landfalling typhoons in China, *Acta Meteorol. Sin.*, **25**, 91– 103.

Wang, M., K. Zhao, M. Xue, G. Zhang, S. Liu, L. Wen, and G. Chen, 2016: Precipitation microphysics characteristics of a Typhoon Matmo (2014) rainband after landfall over eastern China based on polarimetric radar observations, *J. Geophys. Res. Atmos.*, **121**, 12,415–12,433.

Wang, Y., 2009: How do outer spiral rainbands affect tropical cyclone structure and intensity? *J. Atmos. Sci.*, **66**, 1250–1273.

Wang, Z., 2012: Thermodynamic aspects of tropical cyclone formation. *J. Atmos. Sci.*, **69**, 2433–2451.

Wen, L., K. Zhao, G. Chen, M. Wang, B. Zhou, H. Huang, D. Hu, W. –C. Lee, H. Hu, 2018: Drop Size Distribution Characteristics of Seven Typhoons in China. *J. Geophys. Res. Atmos.*, https://doi.org/10.1029/2017JD027950.

Willoughby, H. E., 1978: A possible mechanism for the formation of hurricane rainbands. *J. Atmos. Sci.*, **35**, 838–848.

Wu T., Y. Wan, W. Wo, and L. Leng, 2013. Design and application of radar reflectivity quality control algorithm in SWAN. *Meteor. Sci. Technol.*, **41**: 809-817. (in Chinese with an English abstract)

Yu, C. -K., and C. -L. Tsai, 2010: Surface pressure features of landfalling typhoon rainbands and their possible causes. *J. Atmos. Sci.*, **67**, 2893–2911.

Yuter, S. E., D. E. Kingsmill, L. B. Nance, and M. Löffler-Mang, 2006: Observations of precipitation size and fall speed characteristics within coexisting rain and wet snow. *Journal of Applied Meteorology*, **45**, 1450–1464.

Zawadzki, I., F. Fabry, and W. Szyrmer, 2001: Observations of supercooled water and secondary ice generation by a vertically pointing X-band Doppler radar. *Atmos. Res.*, **59–60**, 343–359.

Zhang, G., J. Vivekanandan, E. A. Brandes, R. Meneghini, and T. Kozu, 2003: The shapeslope relation in observed gamma raindrop size distributions: Statistical error or useful information? *J. Atmos. Oceanic Technol.*, **20**, 1106–1119.

Zhang, G., J. Sun, and E. A. Brandes, 2006: Improving parameterization of rain microphysics with disdrometer and radar observations, *J. Atmos. Sci.*, **63**, 1273–1290.

Table 1. Duration of convective inner-rainband rain (CIR) and convective outer-rainband rain (COR) measured by each disdrometer, with mean values of mass-weighted diameter D_m, normalized intercept parameter $\log_{10}N_w$, and rain rate R.

Station number	Station name	Duration 11 July 2018 (LST)		D_m (mm)		$\log_{10}N_w$ ($mm^{-1}mm^{-3}$)		R ($mm\ h^{-1}$)	
		CIR	COR	CIR	COR	CIR	COR	CIR	COR
1	Shouning	none	0352–1646	0	1.55	0	3.92	0	9.01
2	Zhouning	0830–1030	0409–0829 & 1031–2000	1.54	1.37	3.85	4.22	8.4	11.47
3	Fuan	0800–1040	0321–0759 & 1041–1503	1.48	1.58	3.96	3.96	8.68	10.03
4	Zherong	0800–1040	0231-0759 & 1041–1655	1.69	1.52	4.00	4.06	19.16	13.15
5	Fuding	0512–0729	0237–0511	1.69	1.58	3.92	4.10	15.32	17.40
6	Gutian	0924–1500	1501–2000	1.85	1.62	3.66	3.79	12.45	8.58
7	Xiapu	0400–0750	0244–0359	1.77	1.47	3.92	4.02	18.13	9.21
8	Ningde	0531–1200	1201–1632	1.75	1.30	3.65	4.25	9.75	7.53
9	Pingnan	0857–1300	0608–0856 & 1301–2000	1.63	1.31	3.84	4.23	7.89	9.53

Table 2. Sample numbers, mean values (± sample standard deviations) of rain rate R, radar reflectivity Z, rain water content W, mass-weighted diameter D_m, and normalized intercept parameter $\log_{10}N_w$ for the CIR and COR.

Region	Samples	R ($mm\ h^{-1}$)	Z (dBZ)	W (gm^{-3})	D_m (mm)	$\log_{10}N_w$ ($mm^{-1}mm^{-3}$)
CIR	593	14.67±8.69	40.0±3.5	0.83±0.44	1.72±0.25	3.86±0.24
COR	486	11.19±5.83	37.7±3.3	0.71±0.32	1.51±0.25	4.03±0.26

Figure 1. (a) Track of Typhoon Maria and accumulated rainfall (mm) observed by rain gauges from 1008 LST to 1208 LST 11 July 2018, and (b) intensity of Typhoon Maria from the best track dataset issued by the China Meteorological Administration (CMA). "1108", "1114" and "1120" denote 0800 LST, 1400 LST and 2000 LST 11 July 2018, respectively.

Figure 2. Observed radar reflectivities (dBZ) at Z = 2 km at (a) 0400 LST, (b) 0600 LST and (c) 0838 LST 11 July 2018. The wind field is overlaid on (a). In (b) and (c), the circles indicate the radius of maximum tangential wind (RMW) and 3 RMW at Z = 2 km, both estimated by the T-TREC technique. The blue points indicate the center of Typhoon Maria as determined by the CMA, "IR" and "OR" denote the inner and outer rainbands, the red numbers are the locations of the nine disdrometer sites, and the blue triangle denotes the location of the Ningde radar station (NDRD). In (a), the black lines are radii of length 250 km extending from the TC center, every 5° from 40° to 60° with due west 0°. (d) Radius–time Hovmöller diagram of the azimuthally averaged radar reflectivity (dBZ) from 0300 to 1500 LST 11 July 2018; the black line denotes the evolution of the RMW at Z = 2 km.

Figure 3. (a) As in Figure 2c, but to highlight the convective area with radar reflectivity >32 dBZ as identified by Roger et al. (2013). (b) Average radius–height cross section of reflectivity along the black lines in Figure 2a at 0400 LST 11 July 2018.

Figure 4. Contoured frequency by altitude diagrams (CFADs) of radar reflectivity (dBZ) for (a) CIR and (b) COR. The contour interval is 5%, and the shaded regions indicate values of >20%. The solid thick lines denote the average profiles, and the dashed lines indicate altitudes of 4 and 9 km, and reflectivities of 15 and 30 dBZ.

Figure 5. Scatterplots of rain rate R (mm h^{-1}) versus distance from the TC center for the CIR (red points) and COR (blue points), as the inner and outer rainbands (IR and OR) indicated by Figures 2a–b passed over the observational network from 0330 LST to 0700 LST 11 July 2018.

Figure 6. (a) Scatterplots of the normalized intercept parameter $\log_{10}N_w$ (mm^{-1} m^{-3}) versus the mass-weighted diameter D_m (mm) for the CIR (red points) and COR (blue points) using the rain-type classifcation method modified by Bao et al. (2019). The cyan circle and plus indicate mean values for the CIR and COR, respectively, and contours denote the rain rate (mm h^{-1}; thick contour is 30 mm h^{-1}). The solid line indicates the regression relationship for stratiform rain using the least square fit, and the two rectangles represent the maritime (upper) and continental (lower) convective clusters reported by Bringi et al. (2003). (b) Composite RSDs of CIR (red solid line) and CIR (blue solid line), as well as RSDs of CIR (red dashed line) and CIR (blue dashed line) for rain rate <10 mm h^{-1}.

Figure 7. Evolution of RSD in the (a) CIR and (b) COR as the rain rate increases; the ratio of deviation $[N(D_i)_j–N(D_i)_c]/N(D_i)_c$ between RSD at the jth rain rate and composite RSD with respect to composite RSD for (c) CIR and (d) COR; (e) mean values of total concentration (m^{-3}) and (f) mass-weighted diameter (mm) at different rain rates in the CIR (red bars) and COR (blue bars), as well as the corresponding increase (percentage)

between adjacent rain-rate classes.

Figure 8. Mean values of normalized intercept parameter $\log_{10}N_w$ (mm^{-1} m^{-3}), mass-weighted diameter D_m (mm), and rain rate R (mm h^{-1}) for CIR and COR measured by each disdrometer station. The solid line denotes the locations of Typhoon Maria issued by the CMA every 1 h.

Figure 9. Radial distributions of (a) mass-weighted diameter D_m (mm), (b) normalized intercept parameter $\log_{10}N_w$ (mm^{-1} m^{-3}) and (c) rain rate R (mm h^{-1}) with respect to the radius normalized by RMW (r/RMW) from total samples of CIR (red) and COR (blue) after QC. (d–f) Corresponding box plots with a distance bin of 0.5 RMW from the RMW. The lower and upper ends of the boxes indicate the 25% and 75% values, the bar in the middle is the median value, and other bars (pluses) denote the non-outlier extreme (outlier) values.

Figure 10. Scatterplots of rain rate R (mm h^{-1}) versus normalized intercept parameter $\log_{10}N_w$ (mm^{-1} m^{-3}) for all convective samples after QC (black) and for those within an annular region between 1.5 and 2.5 RMW from the TC center (red). Blue dashed lines denote a rain rate of 30 mm h^{-1} and normalized intercept parameters of 3.8 and 4.2 mm^{-1} m^{-3}.

Figure 11. Scatterplots and corresponding best-fit lines of radar reflectivity Z (mm^{6} m^{-3}) versus rain rate R (mm h^{-1}) for CIR (red) and COR (blue), as well as the best fit lines of previous results reported by Wen et al. (2018) and Bao et al. (2019).

Figure 12. Scatterplots and corresponding best-fit lines of shape parameter μ versus slope parameter Λ (mm^{-1}) for CIR (red) and COR (blue), as well as the best fit lines of previous results reported by Chang et al. (2009), Wen et al. (2018) and Bao et al. (2019).

Figure1.

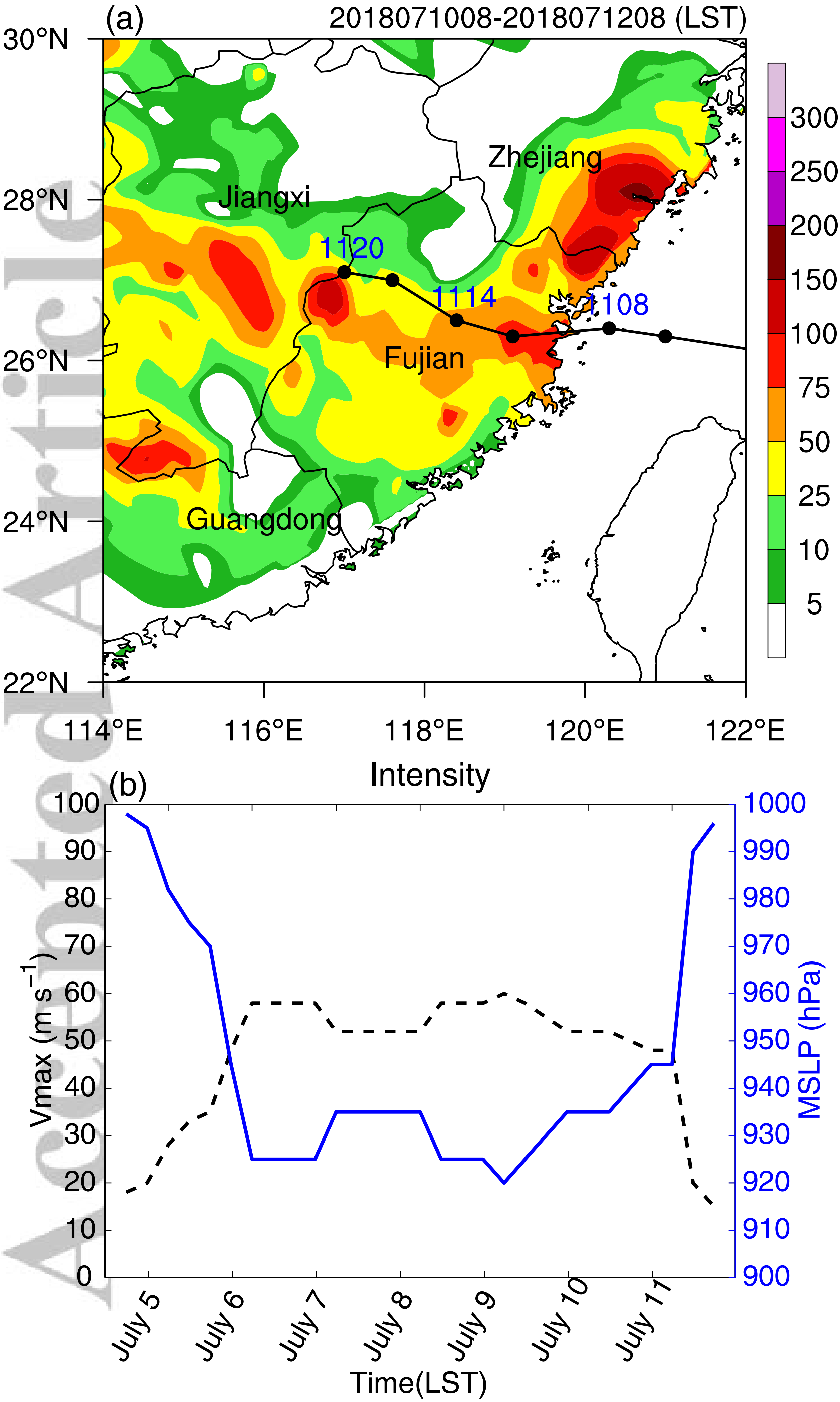
(a)
2018071008-2018071208 (LST)
Zhejiang
Jiangxi
Fujian
Guangdong
1120
1114
1108
30°N
28°N
26°N
24°N
22°N
114°E
116°E
118°E
120°E
122°E
300
250
200
150
100
75
50
25
10
5
Intensity
(b)
Vmax (m s⁻¹)
MSLP (hPa)
July 5
July 6
July 7
July 8
July 9
July 10
July 11
Time(LST)

Figure2.

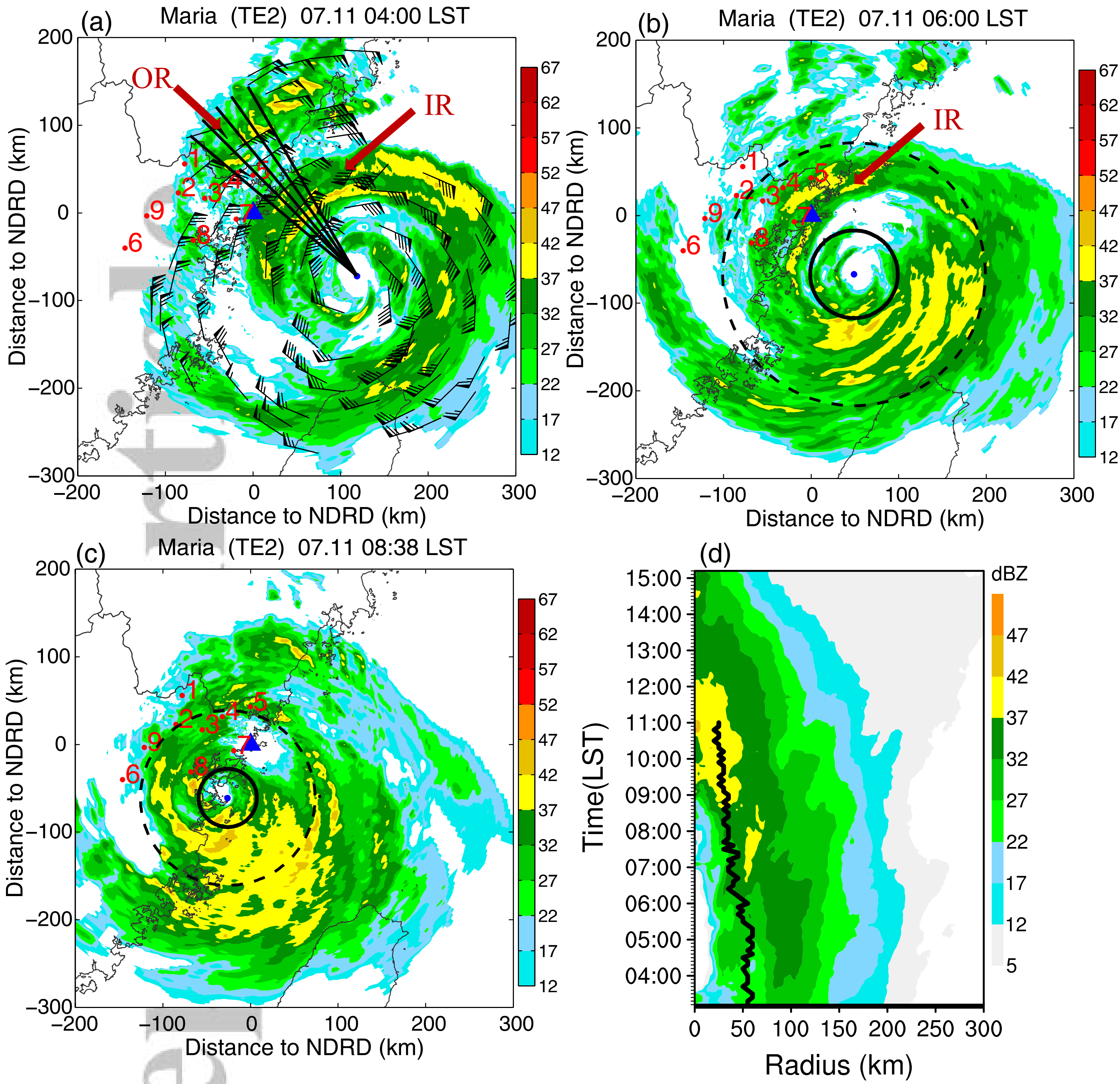

(a)
Maria (TE2) 07.11 04:00 LST
OR
IR
Distance to NDRD (km)
(b)
Maria (TE2) 07.11 06:00 LST
(c)
Maria (TE2) 07.11 08:38 LST
(d)
Time(LST)
Radius (km)
dBZ

Figure3.

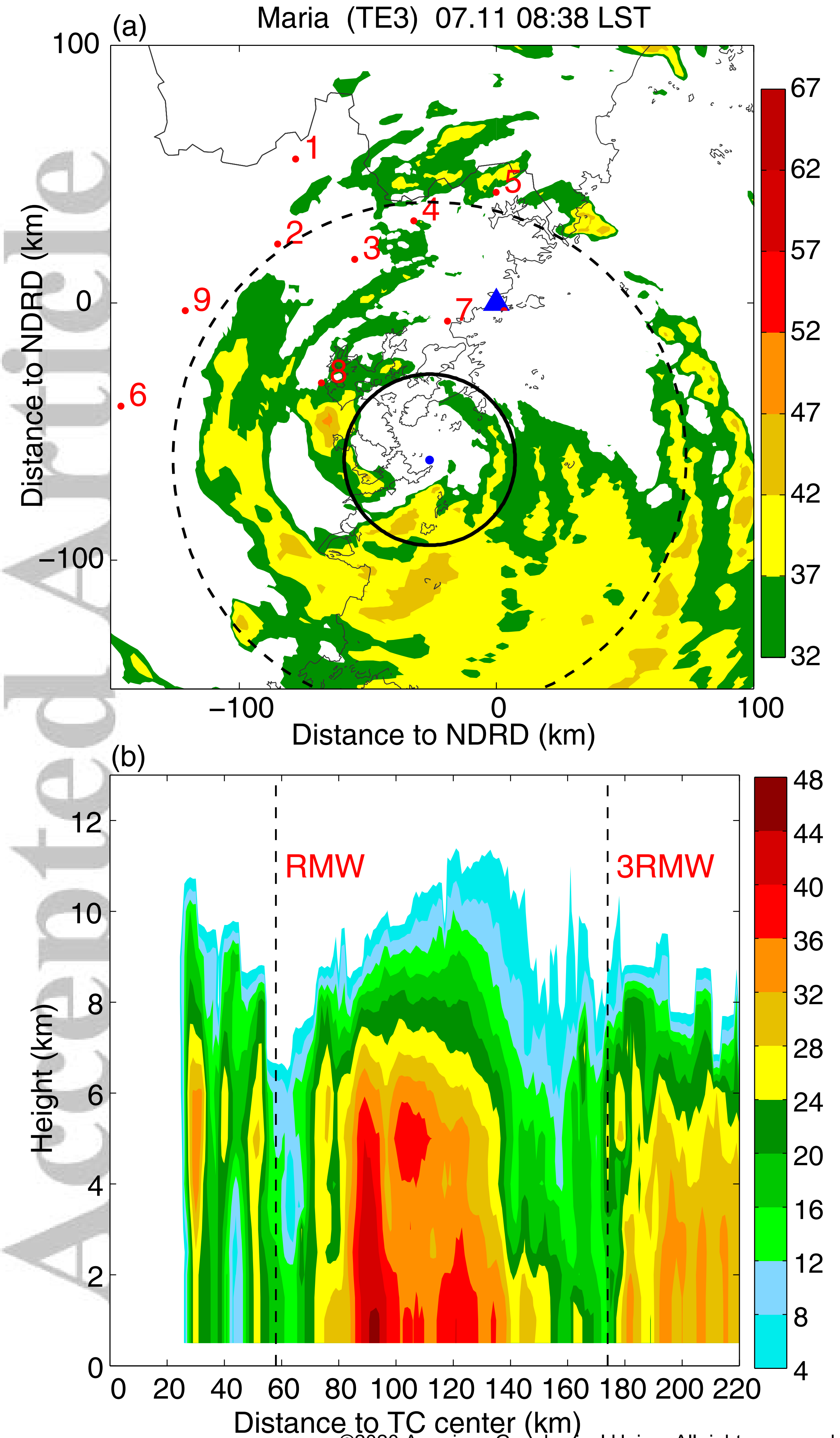

(a)
Maria (TE3) 07.11 08:38 LST
Distance to NDRD (km)
Distance to NDRD (km)
(b)
RMW
3RMW
Height (km)
Distance to TC center (km)

Figure4.

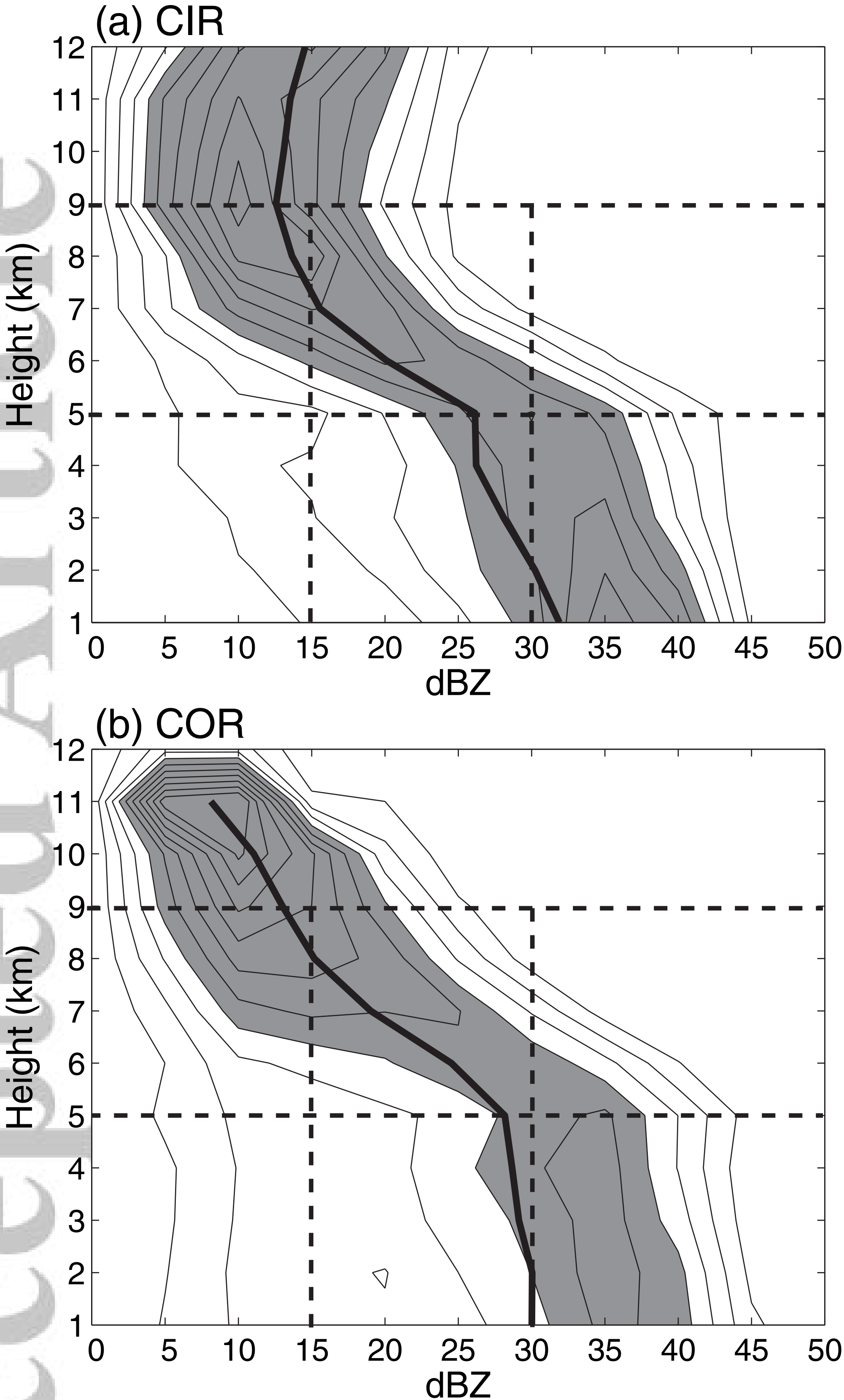
(a) CIR
Height (km)
dBZ
(b) COR
Height (km)
dBZ

Figure5.

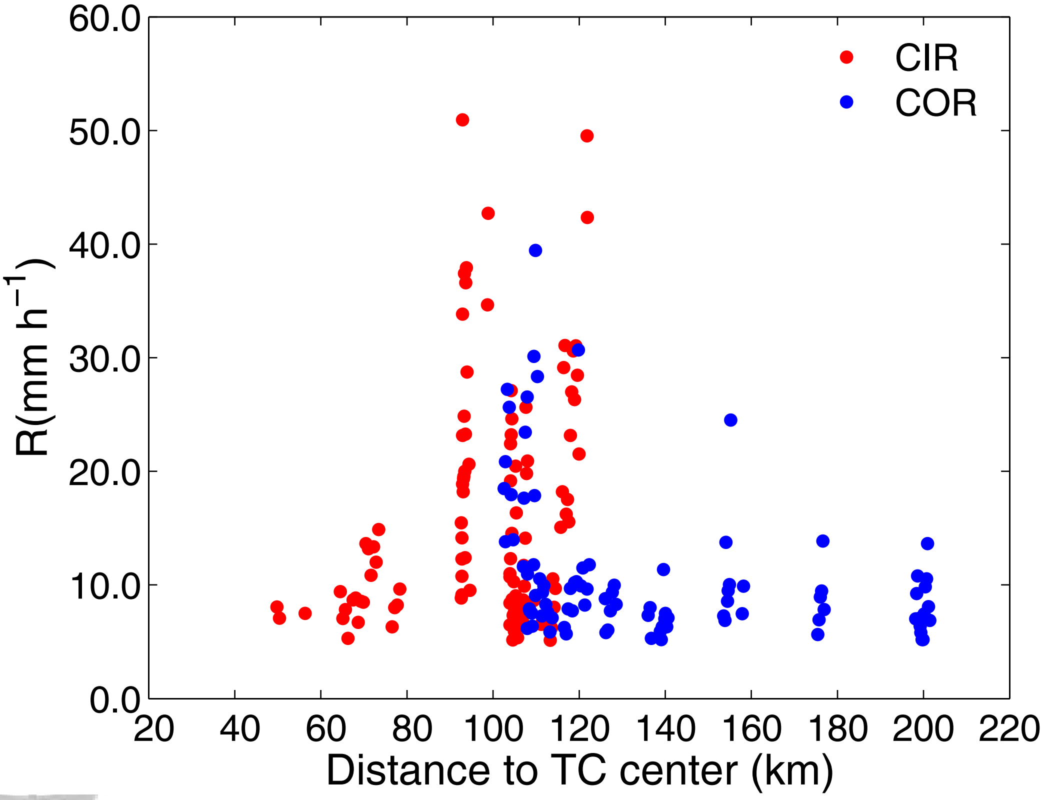
60.0
50.0
40.0
30.0
20.0
10.0
0.0
20
40
60
80
100
120
140
160
180
200
220
Distance to TC center (km)
R(mm h^{-1})
CIR
COR

Figure6.

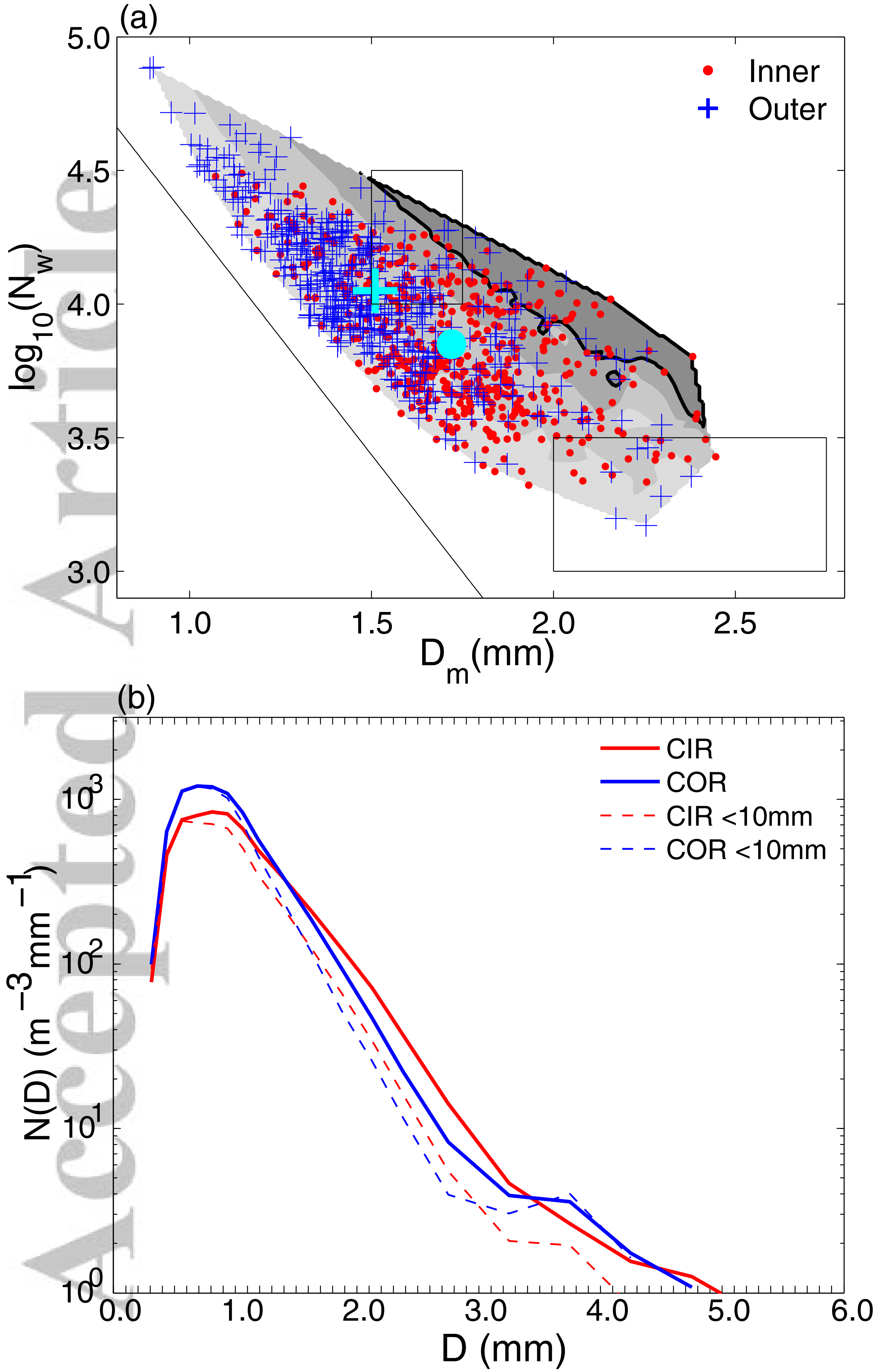

(a)
5.0
4.5
4.0
3.5
3.0
log10(Nw)
1.0
1.5
2.0
2.5
Dm(mm)
Inner
Outer
(b)
CIR
COR
CIR <10mm
COR <10mm
10^3
10^2
10^1
10^0
N(D) (m^−3mm^−1)
0.0
1.0
2.0
3.0
4.0
5.0
6.0
D (mm)

Figure7.

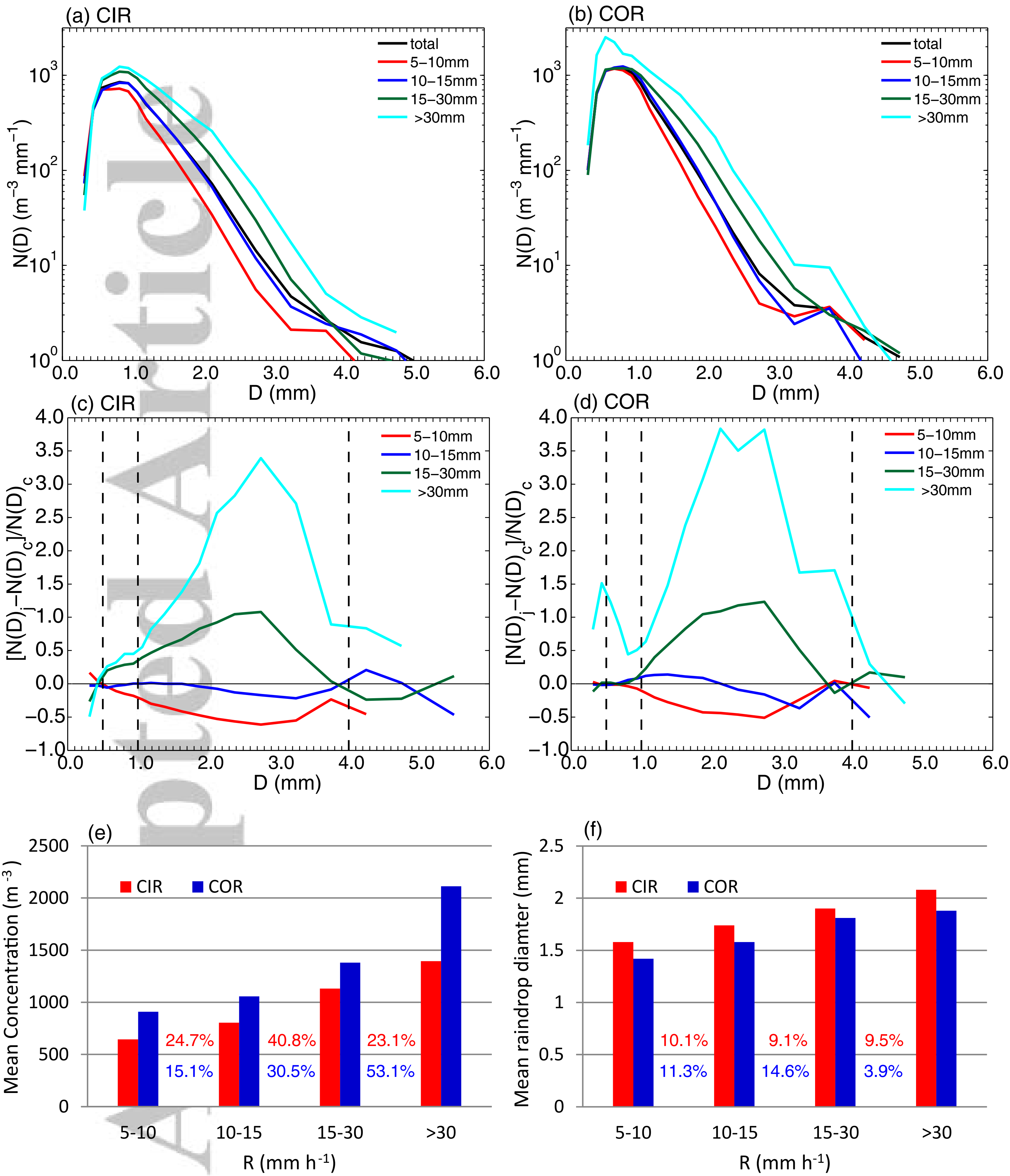

(a) CIR
(b) COR
total
5–10mm
10–15mm
15–30mm
>30mm
N(D) (m^{-3} mm^{-1})
D (mm)
(c) CIR
(d) COR
[N(D)$_j$–N(D)$_c$]/N(D)$_c$
(e)
(f)
CIR
COR
Mean Concentration (m^{-3})
Mean raindrop diamter (mm)
24.7%
15.1%
40.8%
30.5%
23.1%
53.1%
10.1%
11.3%
9.1%
14.6%
9.5%
3.9%
5-10
10-15
15-30
>30
R (mm h^{-1})

Figure8.

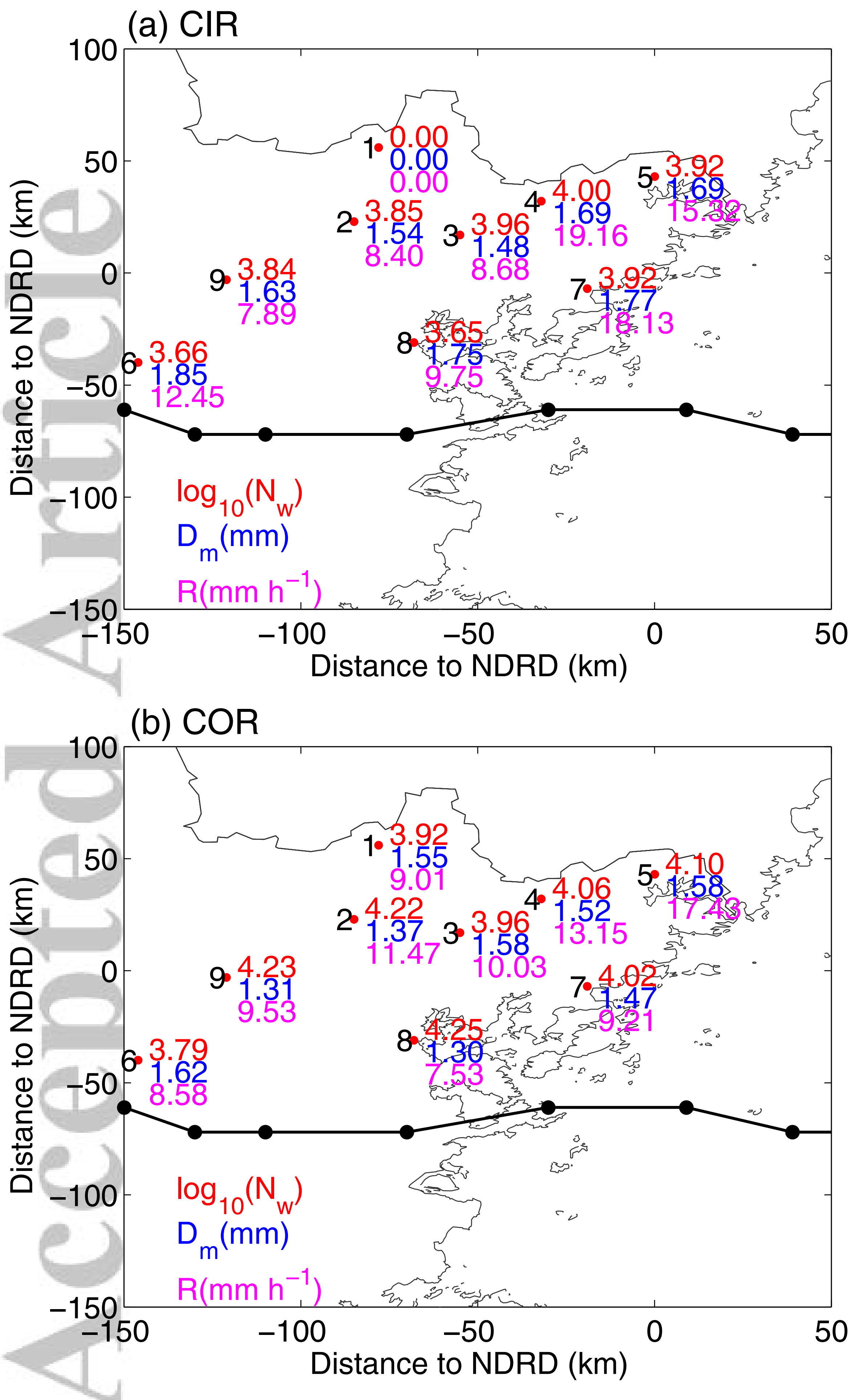
(a) CIR
1 0.00 0.00 0.00
2 3.85 1.54 8.40
3 3.96 1.48 8.68
4 4.00 1.69 19.16
5 3.92 1.69 15.32
6 3.66 1.85 12.45
7 3.92 1.77 18.13
8 3.65 1.75 9.75
9 3.84 1.63 7.89
log10(Nw)
Dm(mm)
R(mm h−1)
Distance to NDRD (km)
Distance to NDRD (km)
(b) COR
1 3.92 1.55 9.01
2 4.22 1.37 11.47
3 3.96 1.58 10.03
4 4.06 1.52 13.15
5 4.10 1.58 17.43
6 3.79 1.62 8.58
7 4.02 1.47 9.21
8 4.25 1.30 7.53
9 4.23 1.31 9.53
log10(Nw)
Dm(mm)
R(mm h−1)
Distance to NDRD (km)
Distance to NDRD (km)

Figure9.

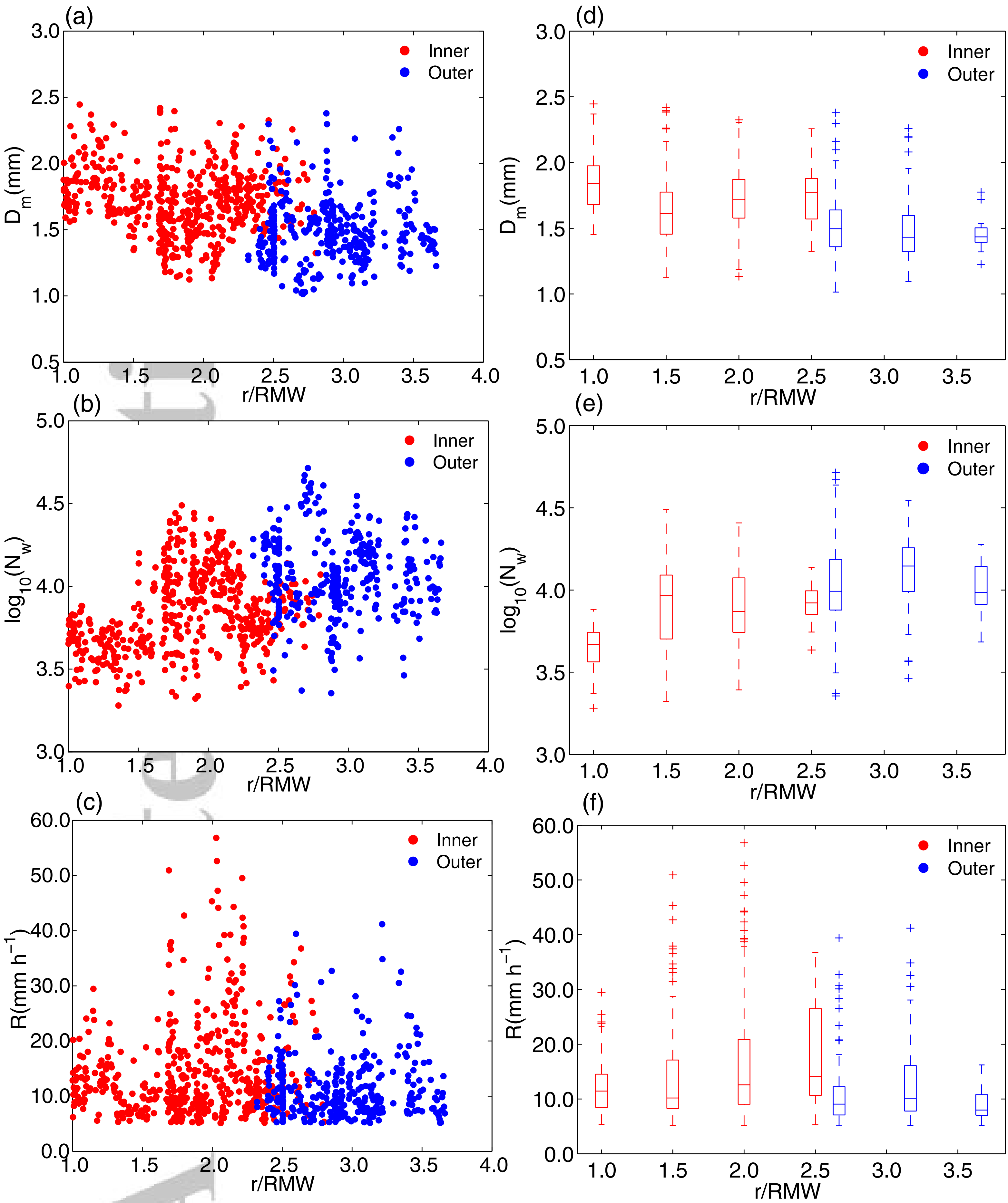
(a)
Inner
Outer
D_m(mm)
r/RMW
(b)
Inner
Outer
log_10(N_w)
r/RMW
(c)
Inner
Outer
R(mm h^-1)
r/RMW
(d)
Inner
Outer
D_m(mm)
r/RMW
(e)
Inner
Outer
log_10(N_w)
r/RMW
(f)
Inner
Outer
R(mm h^-1)
r/RMW

Figure10.

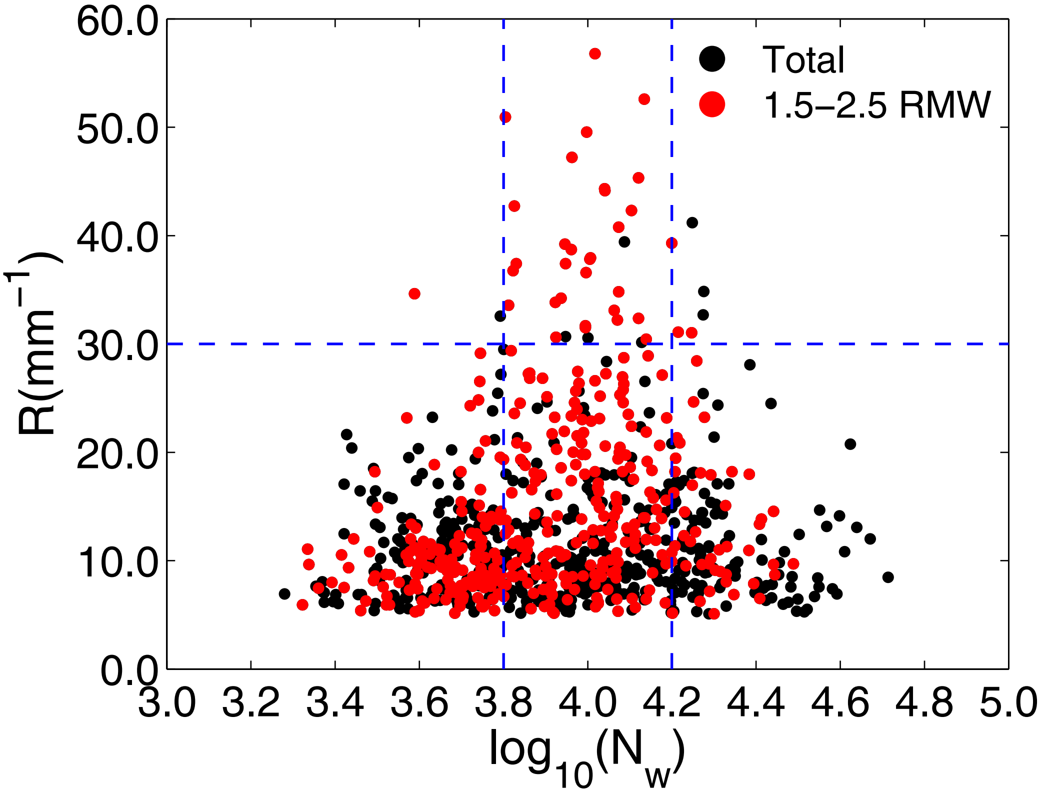

Total
1.5–2.5 RMW
R(mm^{-1})
$\log_{10}(N_w)$
60.0
50.0
40.0
30.0
20.0
10.0
0.0
3.0
3.2
3.4
3.6
3.8
4.0
4.2
4.4
4.6
4.8
5.0

Figure11.

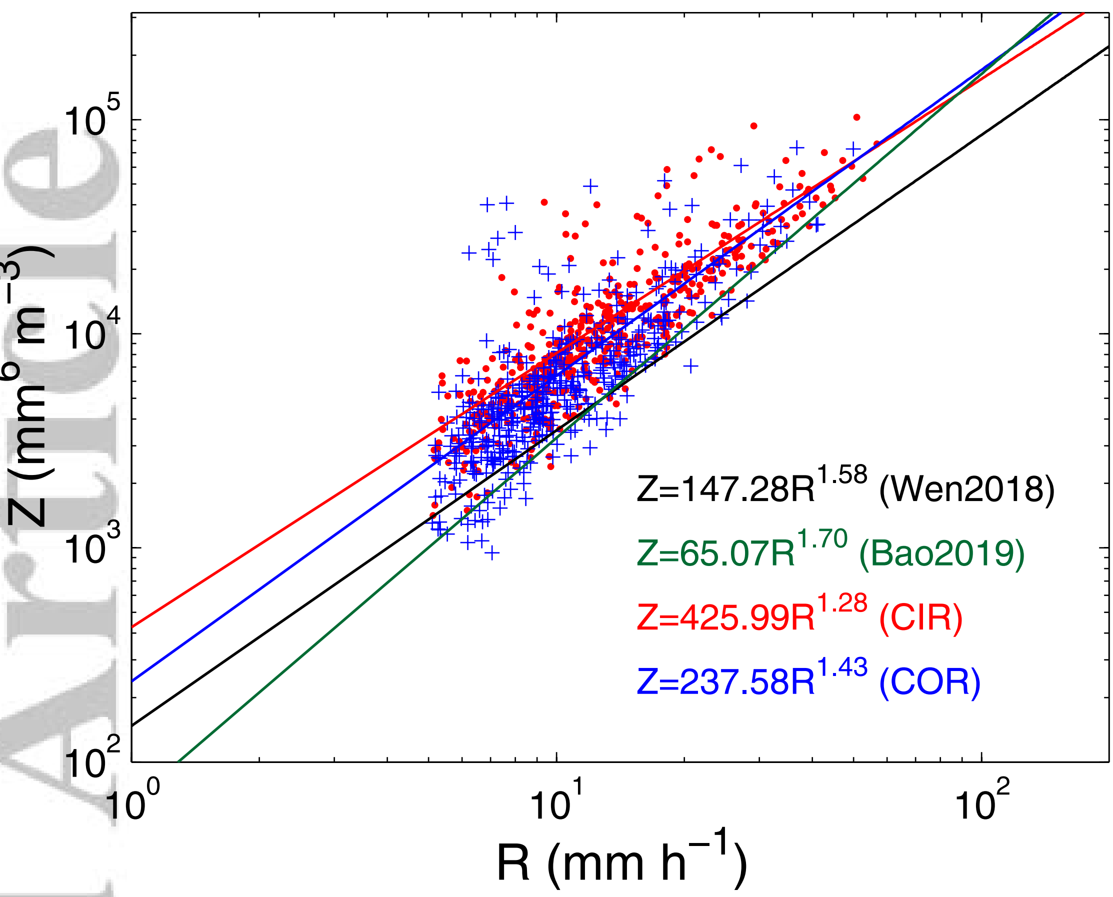
Z (mm^6 m^−3)
R (mm h^−1)
Z=147.28R^1.58 (Wen2018)
Z=65.07R^1.70 (Bao2019)
Z=425.99R^1.28 (CIR)
Z=237.58R^1.43 (COR)

Figure12.

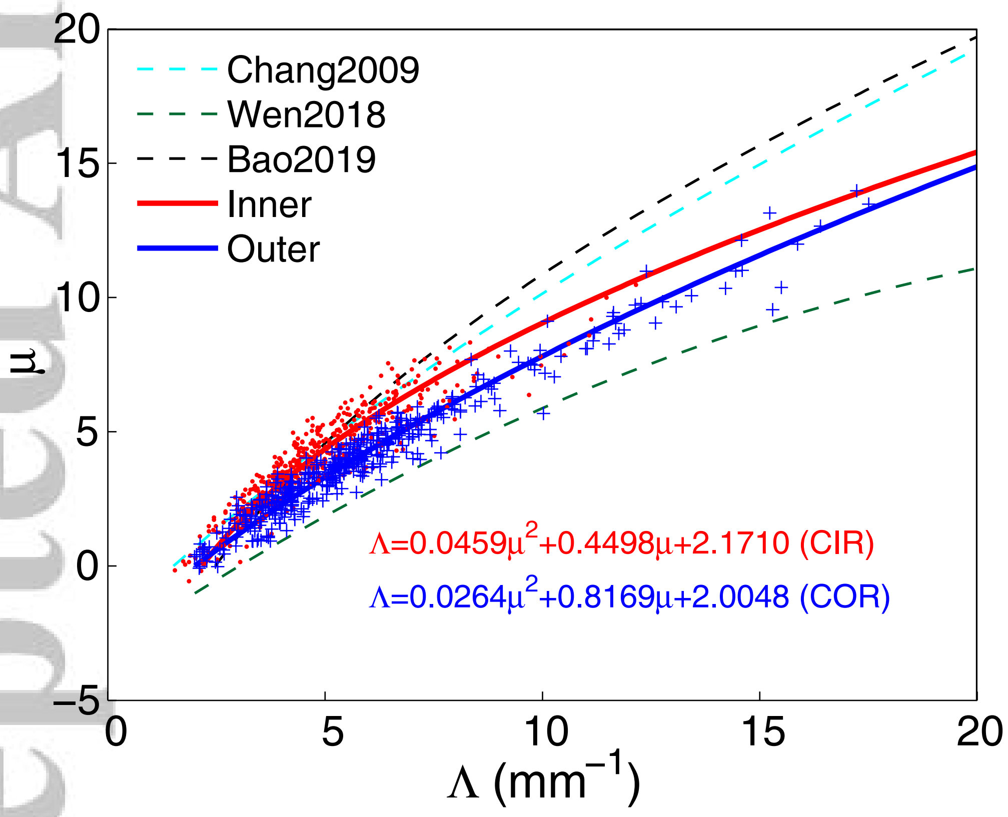

20
15
10
5
0
−5
μ
0
5
10
15
20
Λ (mm^{-1})
Chang2009
Wen2018
Bao2019
Inner
Outer
Λ=0.0459μ^2+0.4498μ+2.1710 (CIR)
Λ=0.0264μ^2+0.8169μ+2.0048 (COR)